AIMS Mathematics, 11(4): 10004–10032.
DOI: 10.3934/math.2026413
Received: 09 February 2026
Revised: 16 March 2026
Accepted: 27 March 2026
Published: 14 April 2026

https://www.aimspress.com/journal/Math

Research article

System-level stability and threshold dynamics of HIV-CTL interactions with intracellular and immune-activation delays

Sayaphat Suksai[1], Suthep Suantai[2,*], Aphisit Tamsat[3] and Chunchom Salikupata[4]

[1] Department of Mathematics, Faculty of Science, Srinakarinwirot University, Bangkok 10110, Thailand
[2] Department of Mathematics, Faculty of Science, Chiang Mai University, Chiang Mai 50200, Thailand
[3] Police Nursing College, Police General Hospital, Royal Thai Police, Bangkok 10330, Thailand
[4] Department of Mathematics, Faculty of Science, King Mongkut's University of Technology Thonburi, Bangkok 10140, Thailand

* **Correspondence:** Email: suthep.s@cmu.ac.th.

Abstract: We formulate and analyze a within-host HIV-CTL model with two biologically motivated discrete delays: an intracellular eclipse delay associated with viral production and a delay in cytotoxic T-lymphocyte activation. While each delay has been studied separately, their combined influence on threshold structure and delay-dependent stability has not been systematically examined in a unified framework. We establish positivity and boundedness of solutions, characterize the infection-free and endemic equilibria, and derive the basic reproduction number together with delay-dependent stability conditions and a Hopf-type transition criterion for the endemic state. Numerically, we perform coarse and high-resolution delay sweeps and construct a two-parameter stability map using viral-load oscillation amplitude as the main diagnostic output. Under the biologically calibrated baseline parameter set, solutions converge to a non-oscillatory chronic state across the physiologically relevant delay ranges explored, and the computed oscillation amplitudes remain numerically negligible. Sensitivity screening and robustness checks further indicate that the infection rate and the CTL activation rate are the dominant drivers of long-term viral burden. These results clarify how intracellular and immune-activation delays shape HIV-CTL dynamics, while showing that delay-induced instability, although possible in principle, is not numerically detected in the baseline regime considered here.

Keywords: HIV-immune system dynamics; cytotoxic T lymphocytes; delayed feedback systems; biomedical system modeling; stability and robustness; immune-mediated control
Mathematics Subject Classification: 34K20, 37G15, 92D30

1. Introduction

Mathematical models of HIV-1 within-host dynamics have long provided key insights into viral replication, immune response, and treatment effects [1–5]. Classical ordinary-differential-equation models quantify target-cell infection, viral production, and clearance [2–6], and subsequent extensions have incorporated cytotoxic T-lymphocyte (CTL) responses and immune escape mechanisms [3–10]. However, these instantaneous models neglect biologically inherent time lags associated with intracellular viral replication and immune activation processes. To capture the delay between cellular infection and progeny virion release, delay-differential-equation (DDE) models with intracellular delays were introduced by Kirschner, Webb, Nelson, and others [11], and were shown to generate damped or sustained viral oscillations [12,13]. Separately, CTL-activation delays have been demonstrated to regulate immune response timing and stability properties [14–16], while spatial heterogeneity has been shown to influence virulence and pathogen evolution in related systems [17]. Yet, existing HIV-CTL models generally include either an intracellular delay or an immune-activation delay, but rarely their combined effects. As a consequence, the joint role of these biologically distinct delays in shaping viral persistence, immune activation, and oscillatory dynamics remains insufficiently understood. Threshold-based analyses using the basic reproduction number R_0 and a secondary CTL-related threshold R_1 provide conditions for viral clearance or persistence in many virus-dynamics models [18–20]. In addition, empirical and theoretical studies have quantified viral growth rates, immune activation mechanisms, and therapy responses in HIV infection [21–23]. Mechanistic modeling of viral-load trajectories and latent-reservoir activation further highlights the complex interplay between infection dynamics, immune responses, and therapeutic interventions [24–27]. Recent developments in delay-differential epidemic and virus-dynamics models have further emphasized the role of time delays in generating stability transitions and bifurcation phenomena [28–30]. In parallel, modern epidemic-model analyses incorporating nonlinear incidence and spatial or structured dynamics provide a broader theoretical framework for understanding threshold behavior and global stability properties in infectious-disease systems [29–31]. These developments motivate the need for refined within-host HIV models that combine multiple biologically meaningful delays within a unified dynamical framework. Treatment effects are typically modeled using a saturating CTL-efficacy function

$$u(A) = u_{max}\frac{A}{(K+A)},$$

where A denotes activated CTLs, $u_{max} \in [0,1]$ is the maximal treatment efficacy, and $K > 0$ is the CTL level at half-maximal efficacy [21,22]. Increasing A therefore enhances treatment potency, and stochastic interplay between immune activation and therapy has been observed in drug-resistance contexts [9,23].

In this work, we close the above gap by formulating a unified two-delay HIV-CTL model that simultaneously incorporates an intracellular (eclipse) delay τ and an immune-activation delay τ_p,

together with an explicit saturating CTL-efficacy function $u(A)$. Denoting by $S(t)$, $I(t)$, $V(t)$, $P(t)$, and $A(t)$ the concentrations of uninfected CD4+ T cells, infected cells, free virions, CTL precursors, and activated CTLs, respectively, the model is given by

$$\dot{S}(t) = \Lambda - \beta S(t)V(t) - \mu S(t) - \alpha P(t)S(t), \tag{1.1}$$

$$\dot{I}(t) = \beta S(t-\tau)V(t-\tau) - dI(t) - u\big(A(t)\big)I(t), \tag{1.2}$$

$$\dot{V}(t) = pI(t) - cV(t) - \eta u\big(A(t)\big)V(t), \tag{1.3}$$

$$\dot{P}(t) = \phi - \rho P(t), \tag{1.4}$$

$$\dot{A}(t) = \sigma P(t-\tau_P) - \kappa A(t). \tag{1.5}$$

Here we formulate an autonomous delay-differential system in which all rate parameters—recruitment (Λ), infection (β), natural death (μ, d), bystander CTL effects (α), virion production (p), viral clearance (c), therapy efficacy modulation (u), CTL precursor turnover (ϕ, ρ), and CTL activation (σ, κ)—are constants, while delays appear only in the state arguments. The contributions of this study are three-fold. First, we establish positivity and boundedness of solutions and characterize the equilibrium structure through the infection-free equilibrium and the endemic equilibrium, together with threshold quantities governing persistence and delay-dependent stability. Second, we derive local stability conditions and a Hopf-type transition criterion for the endemic state, thereby clarifying how the intracellular delay and the immune-activation delay affect the onset of oscillatory behavior in principle. Third, we complement the analytical results with numerical investigations, including coarse and high-resolution delay sweeps, a two-parameter stability map in the (τ, τ_p) plane, a screening-based sensitivity analysis, and targeted robustness checks based on solver tolerances and Euler step-size refinement. The remainder of the paper is organized as follows. Section 2 establishes positivity and boundedness of solutions. Section 3 analyzes the infection-free equilibrium and the endemic equilibria and introduces the threshold quantities relevant to persistence. Section 4 presents the delay-dependent local stability analysis and the Hopf-type transition criterion for the endemic state. Section 5 reports the numerical investigations, including coarse and refined delay sweeps, the two-parameter stability map, sensitivity screening, and robustness checks. Section 6 discusses the biological implications, limitations, and concluding remarks.

Finally, we note that recent delay-structured HIV models incorporating additional transmission pathways and immune mechanisms further confirm the importance of multi-scale dynamical analysis in within-host viral systems [32–35]. The theoretical analysis of delay-differential equations used in this work relies on classical results from the theory of functional differential equations; see Hale and Verduyn Lunel [36] for a comprehensive treatment. In the following section, we establish the positivity and boundedness of solutions of systems (1.1)–(1.5), ensuring the biological feasibility of the model dynamics.

2. Well-posedness, positivity, and ultimate boundedness of solutions

To ensure biological admissibility of systems (1.1)–(1.5), we first establish that solutions initiated from nonnegative histories remain nonnegative and ultimately bounded for all future time. Let

$$C := C([-\max\{\tau, \tau_p\}, 0], \mathbb{R}^5)$$

be the Banach space of continuous history functions equipped with the supremum norm, and define the nonnegative cone

$$C_+ := C([-\max\{\tau, \tau_p\}, 0], \mathbb{R}^5_+).$$

For any initial history $\phi \in C_+$, we prescribe

$$x(\theta) = \phi(\theta), \theta \in [-\max\{\tau, \tau_p\}, 0], \tag{2.1}$$

where $x(t) = (S(t), I(t), V(t), P(t), A(t))$. Since the right-hand side of systems (1.1)–(1.5) is continuous and locally Lipschitz with respect to the state variables, the system admits a unique local solution for every $\phi \in C$. In what follows, we show that C_+ is positively invariant and that every solution initiated in C_+ is ultimately bounded. Consequently, the local solution extends globally on $[0, \infty)$.

Theorem 2.1. (Positive invariance of the nonnegative cone)

If $\phi \in C_+$, then the corresponding solution $x(t)$ of systems (1.1)–(1.5) satisfies

$$x(t) \in \mathbb{R}^5_+, \qquad \forall t \geq 0.$$

Proof. Assume, by contradiction, that some component of $x(t)$ becomes negative for the first time at $t^* > 0$. Then there exists an index $i \in \{1, \ldots, 5\}$ such that

$$x_i(t^*) = 0, x_i(t) \geq 0 \qquad \text{for} \qquad 0 \leq t \leq t^*,$$

and $x_i(t)$ attempts to cross the hyperplane $x_i = 0$ from above at $t = t^*$. Hence, it is enough to verify that the vector field points inward on each boundary face of $\mathbb{R}^5_+$.

If $x_i = S$, then at $S(t^*) = 0$,

$$\dot{S}(t^*) = \Lambda - \beta S(t^*)V(t^*) - \mu S(t^*) - \alpha P(t^*)S(t^*) = \Lambda \geq 0. \tag{2.2}$$

If $x_i = I$, then at $I(t^*) = 0$,

$$\dot{I}(t^*) = \beta S(t^* - \tau)V(t^* - \tau) - dI(t^*) - u(A(t^*))I(t^*) = \beta S(t^* - \tau)V(t^* - \tau) \geq 0, \tag{2.3}$$

because the history remains nonnegative on $[-\max\{\tau, \tau_p\}, t^*]$.

If $x_i = V$, then at $V(t^*) = 0$,

$$\dot{V}(t^*) = pI(t^*) - cV(t^*) - \eta u(A(t^*))V(t^*) = pI(t^*) \geq 0. \tag{2.4}$$

If $x_i = P$, then at $P(t^*) = 0$,

$$\dot{P}(t^*) = \phi - \rho P(t^*) = \phi \geq 0. \tag{2.5}$$

If $x_i = A$, then at $A(t^*) = 0$,

$$\dot{A}(t^*) = \sigma P(t^* - \tau_p) - \kappa A(t^*) = \sigma P(t^* - \tau_p) \geq 0. \tag{2.6}$$

Thus, on every boundary face of $\mathbb{R}^5_+$, the right-hand side of systems (1.1)–(1.5) is nonnegative in the outward normal direction, so no component can cross from nonnegative to negative values. This contradicts the choice of t^*. Therefore,

$$x(t) \in \mathbb{R}^5_+, \forall t \geq 0.$$

The proof is complete.

Theorem 2.2. (Ultimate boundedness and global existence)

For every initial history $\phi \in C_+$, the corresponding solution of systems (1.1)–(1.5) exists for all $t \geq 0$ and is ultimately bounded. More precisely, there exists a constant $M > 0$, independent of t, such that

$$\| x(t) \| \leq M, \qquad \forall t \geq 0. \tag{2.7}$$

Proof. Consider the auxiliary function

$$X(t) = S(t) + I(t) + \gamma V(t) + \delta P(t) + \varepsilon A(t), \tag{2.8}$$

where $\gamma, \delta, \varepsilon > 0$ will be chosen appropriately. Differentiating $X(t)$ along solutions of systems (1.1)–(1.5), we obtain

$$\begin{aligned} \dot{X}(t) = \quad & \Lambda + \delta\phi - \mu S(t) - dI(t) - \gamma c V(t) - \delta\rho P(t) - \varepsilon\kappa A(t) + (\gamma p - 1) I(t) \\ & + (\varepsilon\sigma - \delta\alpha) P(t - \tau_p) - \alpha P(t) S(t) - (\eta\gamma V(t) + I(t)) u(A(t)). \end{aligned} \tag{2.9}$$

We now choose

$$\gamma = \frac{1}{p}, \quad \delta = \frac{\varepsilon\sigma}{\alpha}, \tag{2.10}$$

so that the mixed terms $(\gamma p - 1) I(t)$ and $\left(\varepsilon\sigma - \delta\alpha\right) P(t - \tau_p)$ vanish. Hence,

$$\dot{X}(t) \leq \Lambda + \delta\phi - \mu S(t) - dI(t) - \gamma c V(t) - \delta\rho P(t) - \varepsilon\kappa A(t), \tag{2.11}$$

because the remaining nonlinear terms

$$-\alpha P(t) S(t), -(\eta\gamma V(t) + I(t)) u(A(t))$$

are nonpositive.

Let

$$m = \min \{\mu, d, \gamma c, \delta\rho, \varepsilon\kappa\} > 0. \tag{2.12}$$

Then

$$\dot{X}(t) \leq \Lambda + \delta\phi - mX(t). \tag{2.13}$$

By the comparison principle,

$$X(t) \le X(0)e^{-mt} + \frac{\Lambda+\delta\phi}{m}(1 - e^{-mt}), \tag{2.14}$$

and therefore

$$X(t) \le \max\left\{X(0), \frac{\Lambda+\delta\phi}{m}\right\} =: M_1, \ \forall t \ge 0. \tag{2.15}$$

Since all state variables are nonnegative by Theorem 2.1 and

$$X(t) = S(t) + I(t) + \gamma V(t) + \delta P(t) + \varepsilon A(t),$$

we have

$$0 \le S(t) \le X(t), 0 \le I(t) \le X(t),$$

$$0 \le V(t) \le \frac{X(t)}{\gamma}, \qquad 0 \le P(t) \le \frac{X(t)}{\delta}, \qquad 0 \le A(t) \le \frac{X(t)}{\varepsilon}.$$

Since $X(t) \le M_1$ for all $t \ge 0$, it follows that every component of $x(t)$ is uniformly bounded on $[0, \infty)$. Hence, no finite-time blow-up can occur, and the local solution extends globally. This proves the theorem.

Remark 2.1. Theorem 2.1 guarantees that systems (1.1)–(1.5) preserves biological feasibility, while Theorem 2.2 provides a positively invariant absorbing region in $\mathbb{R}^5_+$. These properties justify the equilibrium and stability analysis developed in the subsequent sections.

3. Equilibrium structure and threshold parameters

We now characterize the equilibrium structure of systems (1.1)–(1.5) and identify the threshold quantities that govern infection establishment and CTL-mediated regulation. In particular, the equilibrium analysis is organized around the infection-free regime and the endemic infection regime, while the auxiliary threshold helps quantify the contribution of CTL-mediated suppression. This leads naturally to two threshold parameters, denoted by R_0 and R_1. Here, R_0 determines viral invasion and persistence, whereas R_1 serves as an auxiliary threshold reflecting intrinsic infection potential in the absence of effective CTL-mediated suppression. An equilibrium is a constant state

$$E^* = (S^*, I^*, V^*, P^*, A^*),$$

satisfying

$$0 = \Lambda - \beta S^* V^* - \mu S^* - \alpha P^* S^*,$$

$$0 = \beta S^* V^* - \big(d + u(A^*)\big) I^*,$$

$$0 = pI^* - \big(c + \eta u(A^*)\big) V^*,$$

$$0 = \phi - \rho P^*,$$

$$0 = \sigma P^* - \kappa A^*. \tag{3.1}$$

Since all parameters are positive, the last two equations immediately give

$$P^* = \frac{\phi}{\rho}, \quad A^* = \frac{\sigma}{\kappa} P^* = \frac{\sigma\phi}{\kappa\rho}. \tag{3.2}$$

Thus, at any equilibrium, the precursor and activated CTL-related components are uniquely determined by the parameter set. Consequently, the equilibrium analysis reduces to the three-dimensional infected subsystem (S^*, I^*, V^*).

When $I^* = V^* = 0$, system (3.1) yields the infection-free equilibrium

$$S^* = \frac{\Lambda}{\mu + \alpha P^*} = \frac{\Lambda}{\mu + \alpha\phi/\rho}. \tag{3.3}$$

Hence,

$$E_0 = \left(\frac{\Lambda}{\mu + \alpha\phi/\rho},\ 0,\ 0,\ \frac{\phi}{\rho},\ \frac{\sigma\phi}{\kappa\rho}\right). \tag{3.4}$$

To quantify the ability of the virus to invade from the infection-free state, we linearize the infected subsystem (I, V) about E_0 and apply the next-generation matrix framework of van den Driessche and Watmough [20]. This yields the basic reproduction number

$$R_0 = \frac{\beta S_0\, p}{(d + u(A_0))(c + \eta u(A_0))} = \frac{\beta\Lambda p}{(\mu + \alpha\phi/\rho)(d + u(A_0))(c + \eta u(A_0))}, \tag{3.5}$$

where

$$S_0 = \frac{\Lambda}{\mu + \alpha\phi/\rho}, \qquad A_0 = \frac{\sigma\phi}{\kappa\rho}.$$

The quantity R_0 measures the average number of newly generated infected cells produced by one infected cell near the infection-free state, after accounting for both infected-cell loss and CTL-mediated viral suppression. Therefore, R_0 governs the primary infection-invasion threshold. When $R_0 > 1$, the virus can persist and a positive infected equilibrium emerges. From the second and third equations of (3.1), for any equilibrium with $I^* > 0$ and $V^* > 0$, we obtain

$$I^* = \frac{\beta S^* V^*}{d + u(A^*)},\ V^* = \frac{pI^*}{c + \eta u(A^*)}. \tag{3.6}$$

Combining these relations gives

$$\beta S^* = \frac{(d + u(A^*))(c + \eta u(A^*))}{p}. \tag{3.7}$$

To quantify the effect of CTL-mediated suppression on infection persistence, we introduce the auxiliary threshold

$$R_1 = \frac{\beta S_0 p}{dc} = \frac{\beta\Lambda p}{(\mu + \alpha\phi/\rho)\, dc}. \tag{3.8}$$

Unlike R_0, the quantity R_1 does not include CTL-mediated clearance terms in the denominator. Thus, R_1 represents the intrinsic infection potential in the absence of effective CTL-mediated suppression, whereas R_0 incorporates immune-mediated viral control through the terms $u(A_0)$ and $\eta u(A_0)$. Since

$$d + u(A_0) \geq d, \qquad c + \eta u(A_0) \geq c,$$

it follows that

$$R_0 \leq R_1.$$

Therefore, R_1 serves as an auxiliary threshold that helps quantify the suppressive contribution of CTL activity, while R_0 remains the actual threshold governing viral invasion and persistence. In particular, $R_0 < 1$ implies that infection cannot invade and the system remains at the infection-free equilibrium, whereas $R_0 > 1$ implies that infection persists and a unique endemic equilibrium exists. This interpretation will be used in the following subsections, while the delay-dependent stability properties of the endemic equilibrium will be analyzed in Section 4.

3.1. Infection-free equilibrium

We first analyze the infection-free equilibrium E_0, which corresponds to the absence of infected cells and free virus. This equilibrium forms the baseline biological state and provides the reference point for defining the viral invasion threshold.

Theorem 3.1. Systems (1.1–1.5) admits the infection-free equilibrium

$$E_0 = (S_0, 0, 0, P_0, A_0), \tag{3.9}$$

where

$$P_0 = \frac{\phi}{\rho}, A_0 = \frac{\sigma\phi}{\kappa\rho}, S_0 = \frac{\Lambda}{\mu+\alpha P_0} = \frac{\Lambda}{\mu+\alpha\frac{\phi}{\rho}}. \tag{3.10}$$

Moreover, following the next-generation matrix framework of van den Driessche and Watmough [20], we define the basic reproduction number

$$R_0 = \frac{\beta S_0 p}{(d+u(A_0))(c+\eta u(A_0))}. \tag{3.11}$$

Then

1) E_0 exists uniquely for all positive parameter values.
2) If $R_0 < 1$, then E_0 is locally asymptotically stable.
3) If $R_0 > 1$, then E_0 is unstable uniquely for all positive parameter values.

Proof. We first establish the existence and uniqueness of the infection-free equilibrium. Setting $I^* = V^* = 0$ in the steady-state system (3.1), the last two equations give

$$0 = \phi - \rho P^*, 0 = \sigma P^* - \kappa A^*, \tag{3.12}$$

from which $P_0 = \frac{\phi}{\rho}$, $A_0 = \frac{\sigma\phi}{\kappa\rho}$. Substituting these expressions into the first equilibrium equation,

$$0 = \Lambda - \mu S^* - \alpha P^* S^*,$$

we obtain

$$0 = \Lambda - (\mu + \alpha P_0) S^*,$$

and hence

$$S_0 = \frac{\Lambda}{\mu + \alpha P_0} = \frac{\Lambda}{\mu + \alpha \phi / \rho}. \tag{3.13}$$

Therefore, E_0 is uniquely determined and exists for all positive parameter values. Next, we analyze the local stability of E_0. Near the infection-free equilibrium, the invasion dynamics are governed by the infected variables $I(t)$ and $V(t)$, while the immune-related variables are fixed at their equilibrium levels P_0 and A_0. Linearizing systems (1.1)–(1.5) about E_0, we obtain the delayed infected subsystem

$$\dot{I}(t) = \beta S_0 V(t-\tau) - (d + u(A_0)) I(t), \dot{V}(t) = pI(t) - (c + \eta u(A_0)) V(t). \tag{3.14}$$

Assuming a solution of the form

$$I(t) = I_1 e^{\lambda t}, V(t) = V_1 e^{\lambda t},$$

we obtain the algebraic system

$$\lambda I_1 = \beta S_0 e^{-\lambda \tau} V_1 - (d + u(A_0)) I_1,$$

$$\lambda V_1 = pI_1 - (c + \eta u(A_0)) V_1.$$

Eliminating I_1 and V_1, the corresponding characteristic equation becomes

$$\lambda^2 + (d + u(A_0) + c + \eta u(A_0))\lambda + (d + u(A_0))(c + \eta u(A_0)) - \beta S_0 p\, e^{-\lambda \tau} = 0. \tag{3.15}$$

Evaluating the characteristic equation at $\lambda = 0$, we obtain

$$(d + u(A_0))(c + \eta u(A_0)) - \beta S_0 p = (d + u(A_0))(c + \eta u(A_0))(1 - R_0). \tag{3.16}$$

Thus, the threshold $R_0 = 1$ determines the transition between decay and invasion of infection.

If $R_0 < 1$, then the effective removal rate of infected cells and free virus dominates the infection production term, so all characteristic roots remain in the left half-plane and E_0 is locally asymptotically stable. On the other hand, if $R_0 > 1$, then the infection production term exceeds the total effective clearance, and the characteristic equation admits an unstable root with a positive real part. Hence, E_0 becomes unstable and infection can invade the system. This completes the proof.

3.2. Endemic equilibrium

We next consider the endemic equilibrium, corresponding to persistent infection with positive infected-cell and viral populations. In the present model, the CTL precursor and activated CTL variables satisfy autonomous balance equations at equilibrium, so their steady-state values are uniquely determined by the parameters and do not generate separate endemic branches.

Consequently, systems (1.1)–(1.5) admits a single biologically relevant endemic equilibrium whenever infection persists

Theorem 3.2. Let

$$P_0 = \frac{\phi}{\rho},\ A_0 = \frac{\sigma\phi}{\kappa\rho}. \tag{3.17}$$

If $R_0 > 1$, then systems (1.1)–(1.5) admits a unique endemic equilibrium

$$E^* = (S^*, I^*, V^*, P_0, A_0), \tag{3.18}$$

where (S^*, I^*, V^*) is the unique positive solution of

$$\beta S^* V^* = \big(d + u(A_0)\big)I^*,$$

$$pI^* = \big(c + \eta u(A_0)\big)V^*,$$

$$\Lambda - (\mu + \alpha P_0)S^* - \beta S^* V^* = 0. \tag{3.19}$$

Proof. At equilibrium, the last two equations of system (3.1) give

$$0 = \phi - \rho P^*, \qquad 0 = \sigma P^* - \kappa A^*,$$

and hence

$$P^* = P_0 = \frac{\phi}{\rho}, \qquad A^* = A_0 = \frac{\sigma\phi}{\kappa\rho}. \tag{3.20}$$

Therefore, any endemic equilibrium must be of the form

$$E^* = (S^*, I^*, V^*, P_0, A_0),$$

with $I^* > 0$ and $V^* > 0$. Substituting P_0 and A_0 into the second and third equilibrium equations yields

$$\beta S^* V^* = (d + u(A_0))I^*, pI^* = (c + \eta u(A_0))V^*. \tag{3.21}$$

Eliminating I^* from these relations, and using $V^* > 0$, we obtain

$$\beta S^* = \frac{(d + u(A_0))(c + \eta u(A_0))}{p},$$

that is,

$$S^* = \frac{(d+u(A_0))(c+\eta u(A_0))}{\beta p}. \tag{3.22}$$

Substituting this into the first equilibrium equation,

$$\Lambda - (\mu + \alpha P_0)S^* - \beta S^* V^* = 0,$$

we solve for V^* as

$$V^* = \frac{\Lambda-(\mu+\alpha P_0)S^*}{\beta S^*}. \tag{3.23}$$

Hence, $V^* > 0$ if and only if

$$\Lambda > (\mu + \alpha P_0)S^*. \tag{3.24}$$

Using the expression for S^* in (3.22), condition (3.24) becomes

$$\Lambda > (\mu + \alpha P_0)\,\frac{(d + u(A_0))(c + \eta u(A_0))}{\beta p},$$

which is equivalent to

$$\frac{\beta \Lambda p}{(\mu + \alpha P_0)(d + u(A_0))(c + \eta u(A_0))} > 1.$$

Therefore,

$$R_0 > 1. \tag{3.25}$$

Once $V^* > 0$, the second relation in (3.21) gives

$$I^* = \frac{c+\eta u(A_0)}{p}\, V^* > 0. \tag{3.26}$$

Thus, under the condition $R_0 > 1$, all equilibrium components are uniquely determined and positive. Conversely, if a positive endemic equilibrium exists, then necessarily $V^* > 0$, so the above argument can be reversed to obtain $R_0 > 1$. Hence, the endemic equilibrium exists uniquely if and only if $R_0 > 1$. This completes the proof.

3.3. Interpretation of the threshold parameters R_0 and R_1

To clarify the role of immune-mediated suppression in the model, we introduce the auxiliary threshold

$$R_1 = \frac{\beta S_0 p}{dc} = \frac{\beta \Lambda p}{(\mu+\alpha\phi/\rho)\, dc}. \tag{3.27}$$

Unlike R_0, the quantity R_1 does not include the CTL-mediated removal terms $u(A_0)$ and $\eta u(A_0)$ in the denominator. Therefore, R_1 represents the intrinsic infection potential in the absence of effective CTL-mediated suppression, whereas R_0 incorporates the reduction of infected cells and free virions due to CTL activity. Since

$$d + u(A_0) \geq d, \qquad c + \eta u(A_0) \geq c,$$

it follows immediately that

$$R_0 \leq R_1. \tag{3.28}$$

Thus, the difference between R_1 and R_0 quantifies the suppressive contribution of the CTL efficacy function $u(A)$ at equilibrium. In particular, the closer R_0 is to R_1, the weaker the effective CTL-mediated reduction in viral persistence; conversely, a larger separation between R_1 and R_0 reflects

stronger immune-mediated suppression. Accordingly, R_0 remains the principal threshold governing viral invasion and persistence, whereas R_1 serves as an auxiliary threshold that isolates the contribution of CTL-mediated suppression by removing the terms involving $u(A_0)$ from the effective clearance rates. If $R_0 < 1$, infection cannot invade and the infection-free equilibrium E_0 is locally stable. If $R_0 > 1$, infection persists and the model admits the unique endemic equilibrium E^*, whose delay-dependent stability properties are analyzed in Section 4.

Therefore, in the present model, R_0 determines the actual invasion and persistence threshold, while R_1 serves as an auxiliary indicator for assessing how strongly CTL activity modifies the underlying infection potential. This interpretation is consistent with the equilibrium structure derived above; the model admits one infection-free equilibrium and one endemic equilibrium, while the pair (R_0, R_1) helps explain how immune regulation reshapes the effective reproductive capacity of the virus.

4. Stability analysis

In this section, we investigate the local stability of the biologically relevant equilibria of systems (1.1)–(1.5), namely, the infection-free equilibrium E_0 and the endemic equilibrium E^*. The stability analysis of delay differential systems follows classical results in functional differential equations (see Hale and Verduyn Lunel [36]). Our analysis shows that the basic reproduction number R_0 determines the infection-persistence threshold, while the intracellular delay τ governs the onset of instability and possible Hopf bifurcation. By contrast, the immune-activation delay τ_p affects the transient immune-response dynamics.

4.1. Stability of the infection-free equilibrium E_0

Recall from Section 3 that

$$E_0 = (S_0, 0, 0, P_0, A_0), S_0 = \frac{\Lambda}{\mu + \alpha P_0}, P_0 = \frac{\phi}{\rho}, A_0 = \frac{\sigma\phi}{\kappa\rho}.$$

Linearizing systems (1.1)–(1.5) about E_0, we observe that the (S, P, A) modes are decoupled from the infected block (I, V). The corresponding eigenvalues associated with the (S, P, A) subsystem are

$$-(\mu + \alpha P_0), \qquad -\rho, \qquad -\kappa,$$

which are all strictly negative. Therefore, the local stability of E_0 is determined entirely by the delayed infected subsystem

$$\dot{I}(t) = \beta S_0 V(t-\tau) - (d + u(A_0))I(t), \qquad \dot{V}(t) = pI(t) - (c + \eta u(A_0))V(t).$$

Assuming exponential solutions of the form $e^{\lambda t}$, we obtain the characteristic equation

$$\lambda^2 + \big(d + u(A_0) + c + \eta u(A_0)\big)\lambda + \big(d + u(A_0)\big)\big(c + \eta u(A_0)\big) = \beta S_0 p e^{-\lambda\tau}. \tag{4.1}$$

Define

$$R_0 = \frac{\beta S_0 p}{(d+u(A_0))(c+\eta u(A_0))}. \tag{4.2}$$

By classical stability theory for delay-differential equations (see Hale and Verduyn Lunel [36]), together with the threshold characterization obtained in Section 3, the infection-free equilibrium E_0 is locally asymptotically stable if $R_0 < 1$, and unstable if $R_0 > 1$.

4.2. Stability of the endemic equilibrium E^*

We next examine the endemic equilibrium

$$E^* = (S^*, I^*, V^*, P_0, A_0),$$

which exists uniquely when $R_0 > 1$. At this equilibrium, the immune-related components remain fixed at their equilibrium levels P_0 and A_0, while the infected-cell and viral populations are positive. Linearizing systems (1.1)–(1.5) about E^*, the (P, A) subsystem again contributes stable modes associated with the eigenvalues

$$-\rho, \qquad -\kappa.$$

The remaining stability behavior is governed by the coupled delayed subsystem involving S, I, and V. Because the intracellular delay enters through the infection term, the characteristic equation at E^* takes a delay-dependent transcendental form. In general, this equation cannot be reduced to the same threshold expression as for E_0. The local stability of E^* for small delays, as well as the possible delay-induced loss of stability, will be examined through the characteristic equation in the next subsection. To make this dependence explicit, we derive the corresponding characteristic equation and then determine the conditions under which Hopf bifurcation occurs.

4.3. Hopf bifurcation at the endemic equilibrium E^*

To investigate delay-induced loss of stability at the endemic equilibrium E^*, we linearize systems (1.1)–(1.5) about

$$E^* = (S^*, I^*, V^*, P_0, A_0),$$

where $P_0 = \phi/\rho$ and $A_0 = \sigma\phi/(\kappa\rho)$. Let

$$S(t) = S^* + x_1(t), \qquad I(t) = I^* + x_2(t), \qquad V(t) = V^* + x_3(t),$$

$$P(t) = P_0 + x_4(t), \qquad A(t) = A_0 + x_5(t),$$

where $x_i(t), \quad i = 1, \dots, 5,$ are sufficiently small perturbations. Substituting these expressions into systems (1.1)–(1.5) and neglecting higher-order terms, we obtain the linearized system

$$\dot{x}_1(t) = -(\beta V^* + \mu + \alpha P_0)x_1(t) - \beta S^* x_3(t) - \alpha S^* x_4(t), \tag{4.3}$$

$$\dot{x}_2(t) = \beta V^* x_1(t-\tau) + \beta S^* x_3(t-\tau) - (d + u(A_0))x_2(t) - u'(A_0)I^* x_5(t), \tag{4.4}$$

$$\dot{x}_3(t) = p x_2(t) - (c + \eta u(A_0))x_3(t) - \eta u'(A_0)V^* x_5(t), \tag{4.5}$$

$$\dot{x}_4(t) = -\rho x_4(t), \tag{4.6}$$

$$\dot{x}_5(t) = \sigma x_4(t-\tau_p) - \kappa x_5(t). \tag{4.7}$$

From (4.6)–(4.7) the (x_4, x_5) subsystem is decoupled from (x_1, x_2, x_3). Therefore, the corresponding characteristic factor is

$$(\lambda + \rho)(\lambda + \kappa) = 0, \tag{4.8}$$

so the eigenvalues associated with the P and A components are always negative. Hence, the local stability of E^* is determined entirely by the (x_1, x_2, x_3) subsystem. In particular, the immune-activation delay τ_p does not enter the characteristic equation governing the local stability of E^*. For the subsystem (x_1, x_2, x_3), we seek solutions of the form

$$x_j(t) = \xi_j e^{\lambda t}, \qquad j = 1,2,3.$$

Substituting into (4.3)–(4.5), we obtain the algebraic system

$$(\lambda + \beta V^* + \mu + \alpha P_0)\xi_1 + \beta S^* \xi_3 = 0,$$
$$-\beta V^* e^{-\lambda\tau}\xi_1 + (\lambda + d + u(A_0))\xi_2 - \beta S^* e^{-\lambda\tau}\xi_3 = 0,$$
$$-p\xi_2 + (\lambda + c + \eta u(A_0))\xi_3 = 0.$$

Thus, the characteristic equation is

$$\det \begin{pmatrix} \lambda + \beta V^* + \mu + \alpha P_0 & 0 & \beta S^* \\ -\beta V^* e^{-\lambda\tau} & \lambda + d + u(A_0) & -\beta S^* e^{-\lambda\tau} \\ 0 & -p & \lambda + c + \eta u(A_0) \end{pmatrix} = 0. \tag{4.9}$$

Expanding the determinant gives

$$(\lambda + \beta V^* + \mu + \alpha P_0)(\lambda + d + u(A_0))(\lambda + c + \eta u(A_0)) - \beta S^* p\, e^{-\lambda\tau}(\lambda + \mu + \alpha P_0) = 0. \tag{4.10}$$

For convenience, define

$$a_1 = \beta V^* + \mu + \alpha P_0, \qquad a_2 = d + u(A_0), \qquad a_3 = c + \eta u(A_0),$$
$$b_1 = \beta S^* p, \quad b_0 = \beta S^* p(\mu + \alpha P_0).$$

Then (4.10) can be rewritten as

$$\lambda^3 + A_1\lambda^2 + A_2\lambda + A_3 - (b_1\lambda + b_0)e^{-\lambda\tau} = 0, \tag{4.11}$$

with

$$A_1 = a_1 + a_2 + a_3, \qquad A_2 = a_1a_2 + a_1a_3 + a_2a_3, \qquad A_3 = a_1a_2a_3.$$

To determine the onset of Hopf bifurcation, we look for purely imaginary roots of the form

$$\lambda = i\omega, \ \omega > 0. \tag{4.12}$$

Substituting $\lambda = i\omega$ into (4.11), and separating the real and imaginary parts, yields

$$-A_1\omega^2 + A_3 - b_0\cos(\omega\tau) - b_1\omega\sin(\omega\tau) = 0, \tag{4.13}$$
$$-\omega^3 + A_2\omega - b_1\omega\cos(\omega\tau) + b_0\sin(\omega\tau) = 0. \tag{4.14}$$

Squaring (4.13) and (4.14), and then adding the resulting equations, we eliminate the trigonometric terms and obtain

$$(A_3 - A_1\omega^2)^2 + (A_2\omega - \omega^3)^2 = b_0^2 + b_1^2\omega^2. \tag{4.15}$$

Equivalently,

$$\omega^6 + (A_1^2 - 2A_2)\omega^4 + (A_2^2 - 2A_1A_3 - b_1^2)\omega^2 + (A_3^2 - b_0^2) = 0. \tag{4.16}$$

Suppose that (4.16) admits a positive root $\omega_0 > 0$. Then the corresponding critical delay values are determined from (4.13) and (4.14). In particular,

$$\cos(\omega_0\tau_0) = \frac{b_0(A_3 - A_1\omega_0^2) + b_1\omega_0(A_2\omega_0 - \omega_0^3)}{b_0^2 + b_1^2\omega_0^2}, \tag{4.17}$$

and hence

$$\tau_0^{(n)} = \frac{1}{\omega_0}\arccos\left(\frac{b_0(A_3 - A_1\omega_0^2) + b_1\omega_0(A_2\omega_0 - \omega_0^3)}{b_0^2 + b_1^2\omega_0^2}\right) + \frac{2n\pi}{\omega_0}, n = 0,1,2,\ldots \tag{4.18}$$

Therefore, if Eq (4.16) has a positive root ω_0, then the characteristic Eq (4.11) has a pair of purely imaginary roots $\pm i\omega_0$ at $\tau = \tau_0^{(n)}$. To verify Hopf bifurcation, it remains to impose the transversality condition

$$\frac{d\,\Re(\lambda(\tau))}{d\tau}\Big|_{\tau=\tau_0^{(n)}} \neq 0. \tag{4.19}$$

Under this condition, the pair of characteristic roots crosses the imaginary axis with nonzero speed as τ passes through $\tau_0^{(n)}$. Hence, by the Hopf bifurcation theorem for delay-differential equations, the endemic equilibrium E^*undergoes a Hopf bifurcation at $\tau = \tau_0^{(n)}$.

We summarize the result as follows.

Theorem 4.1. Assume that $R_0 > 1$, so that the endemic equilibrium E^* exists uniquely. If Eq (4.16) admits a positive root $\omega_0 > 0$, and the transversality condition (4.19) holds at the corresponding critical delay value $\tau_0^{(n)}$, then the endemic equilibrium E^* loses stability through a Hopf bifurcation at $\tau = \tau_0^{(n)}$. Consequently, a family of periodic solutions bifurcates from E^*.

Proof. From the linearization of systems (1.1)–(1.5) about E^*, the characteristic equation is given by (4.11). Let $\lambda = i\omega$, $\omega > 0$. Substituting this form into (4.11) and separating the real and imaginary parts yields Eqs (4.13)–(4.14). Eliminating the trigonometric terms leads to the auxiliary Eq (4.16). Hence, if (4.16) admits a positive root ω_0, then the characteristic equation possesses a pair of purely imaginary roots $\lambda = \pm i\omega_0$ for $\tau = \tau_0^{(n)}$, where $\tau_0^{(n)}$ is determined by (4.18).

If, in addition, the transversality condition (4.19) holds, then the real part of the corresponding characteristic roots changes sign as τ passes through $\tau_0^{(n)}$. Therefore, the pair of characteristic roots crosses the imaginary axis with nonzero speed. By the Hopf bifurcation theorem for delay-differential equations, the endemic equilibrium E^* undergoes a Hopf bifurcation at $\tau = \tau_0^{(n)}$, and a branch of periodic solutions emerges from E^*. This completes the proof.

The above result shows that delay-induced oscillations in the endemic regime arise through the intracellular delay τ. By contrast, the immune-activation delay τ_p does not influence the local stability boundary, since it does not appear in the characteristic equation of the reduced (x_1, x_2, x_3) subsystem.

5. Numerical simulations

In this section, we corroborate the theoretical thresholds R_0 and R_1 and the delay-dependent stability results established in Sections 3–4 through numerical simulations of system (1.1)–(1.5). All baseline parameter values and literature sources used in this section are summarized in Table 1, and unless otherwise stated, these values remain fixed across all experiments to ensure consistent comparability between analytical and numerical results. We adopt the CTL-efficacy function

$$u(A) = \frac{u_{max}A}{K+A}, \quad u_{max} = 1, \ K = 50 \tag{5.1}$$

and set the history functions on $[-max(\tau, \tau_P), 0]$ to constant values at the infection-free equilibrium $(S_0, I_0, V_0, P_0, A_0)$. Although constant history functions are used for numerical consistency, the simulations still capture the threshold behavior and delay-dependent dynamics predicted by the analytical results. Numerical integrations are performed in two complementary layers: a coarse delay survey to explore the parameter window in which oscillatory behavior may arise, followed by a high-resolution refinement using dde23 to obtain more precise dynamical information and accurate estimates of critical delay values. In the infection-free regime $(R_0 < 1)$, both infected-cell density $I(t)$ and viral load $V(t)$ decay monotonically to zero, while uninfected CD4+ T cells recover to S_0, confirming convergence to the infection-free equilibrium E_0, in agreement with the analytical result in Section 4.1. In the endemic regime $(R_0 > 1)$, solutions converge to the endemic equilibrium E^* when the intracellular delay τ remains below its critical threshold. As τ increases beyond the critical value, oscillatory transients or sustained oscillations may emerge, reflecting delay-induced destabilization through the Hopf bifurcation mechanism described in Section 4.3. By contrast, the immune-activation delay τ_p does not alter the local stability boundary, although it may influence the transient response of the CTL-related variables.

Table 1 summarizes the baseline parameter values and their literature sources used in all numerical experiments in Section 5, covering both time-course simulations and delay-sweep analyses. Except where noted otherwise, these baseline values remain fixed across simulations, while the delay parameters τ and τ_p are varied depending on the scenario being examined.

Table 1. Baseline parameter values and literature sources used in the numerical simulations.

Parameter	Description	Value	Reference
Λ	$CD4^+$ T-cell production rate	10 cells·ml^{-1}·day^{-1}	[1]
μ	Natural death rate of uninfected $CD4^+$ T cells	0.1 day^{-1}	[1]
β	Infection rate constant	5×10^{-4} ml·virion^{-1}·day^{-1}	[6]
d	Death rate of infected $CD4^+$ T cells	0.5 day^{-1}	[1]
p	Virion production per infected cell	100 virions·cell^{-1}·day^{-1}	[4]
c	Virion clearance rate	2 day^{-1}	[4]
ϕ	CTL-precursor source rate	5 cells·day^{-1}	[13]
ρ	CTL-precursor death rate	0.2 day^{-1}	[13]
σ	Rate of CTL activation from precursors	0.3 day^{-1}	[13]
κ	Death rate of activated CTLs	0.1 day^{-1}	[13]
α	CTL bystander effect on uninfected cells	0.01 ml·cell^{-1}·day^{-1}	[10]
η	CTL-mediated enhancement of viral clearance	0.5 (–)	[10]
u_{max}	Maximum treatment efficacy	1 (–)	[11]
K	CTL level giving half-maximum efficacy in $u(A) = u_{max}A/(K + A)$	50 cells·ml^{-1}	[11]

Figure 1 illustrates the time-course trajectories of infected-cell density $I(t)$ (top) and viral load $V(t)$ (bottom) under five representative parameter regimes. In Case 1, where $R_0 < 1$, both $I(t)$ and $V(t)$ decay to zero, confirming convergence to the infection-free equilibrium E_0. In the remaining cases, corresponding to endemic parameter settings, the solutions exhibit either convergence to the endemic equilibrium E^* or oscillatory transient behavior as the intracellular delay τ increases. Variations in τ_p affect transient immune-response dynamics, but do not alter the local stability boundary.

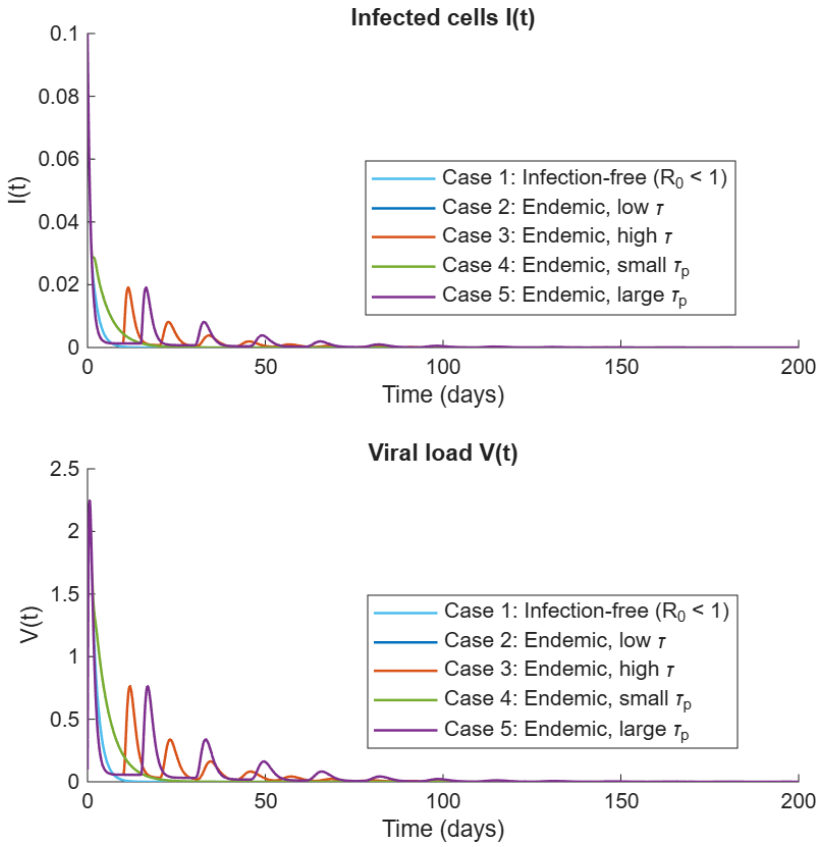

Figure 1. Dynamics of infected CD4+ T cells and viral load under five representative parameter regimes.

Remark. Only $I(t)$ and $V(t)$ are shown because they directly quantify infection dynamics; the uninfected-cell and CTL-related compartments (S, P, A) remain close to their equilibrium levels after transients and provide comparatively limited additional visual information.

5.1. Materials and methods

5.1.1. Model formulation

The model Eqs (1.1)–(1.5) defined in the Introduction describe the dynamics of five state variables—susceptible CD4$^+$ T cells S, infected CD4$^+$ T cells I, free virus V, CTL precursors P, and activated CTLs A. The model incorporates two discrete delays: the intracellular infection delay τ and the CTL-activation delay τ_p. We retain the original model structure and the treatment term $u(A)$ introduced earlier. Baseline parameter values and treatment-related constants used in the numerical experiments are summarized in Table 1. For delay simulations, history functions on $[-\max(\tau, \tau_p), 0]$ were specified as constant values consistent with the infection-free equilibrium $(S_0, I_0, V_0, P_0, A_0)$, where small perturbations $I_0 > 0$ and $V_0 > 0$ were introduced to initiate infection dynamics. The numerical procedures for the coarse and refined delay sweeps are described in Sections 5.1.2–5.1.3.

5.1.2. Numerical simulations and coarse bifurcation analysis

To obtain an overview of the influence of the intracellular delay τ on systems (1.1)–(1.5), we performed a coarse delay sweep using a fixed-step Euler method. Simulations were conducted with step size $h = 0.5$ days and solutions were computed over $t \in [0,50]$ days, with history functions on $[-\max(\tau, \tau_p), 0]$ fixed near the infection-free equilibrium $(S_0, I_0, V_0, P_0, A_0)$. We varied τ from 0.5 to 50 days in increments of 2 days and recorded the corresponding trajectory of the viral load $V(t)$. To reduce the effect of transient dynamics, the initial portion of each simulation was discarded. The oscillation amplitude of $V(t)$ was then computed as

$$A_{\text{osc}} = \max_{t \geq T_0} V(t) - \min_{t \geq T_0} V(t), \tag{5.2}$$

where T_0 denotes the end of the transient phase. The resulting amplitude-τ relationship was used to construct a coarse bifurcation-like diagram, which guided the selection of delay regions for refined analysis in Section 5.1.3.

5.1.3. High-resolution DDE solver

Guided by the coarse bifurcation results in Section 5.1.2, we performed refined delay sweeps using MATLAB's built-in dde23 solver. For each selected value of the intracellular delay τ in the region of interest, system (1.1)–(1.5) was integrated over a sufficiently long-time horizon to capture post-transient behavior. Solver tolerances were set to $\text{AbsTol} = 10^{-6}$ and $\text{RelTol} = 10^{-4}$, with $\text{MaxStep} = 1.0$ day. History functions on $[-\max(\tau, \tau_p), 0]$ were held constant at $(S_0, I_0, V_0, P_0, A_0)$. Oscillation amplitudes of $V(t)$ were quantified from the stabilized portion of the trajectories using the difference between the observed maxima and minima. These high-resolution computations provide more accurate estimates of the delay-dependent transition structure and support the numerical bifurcation diagrams reported in Sections 5.2–5.3.

5.2. Coarse bifurcation diagram

Using the amplitude measure defined in Section 5.1.2, we constructed a coarse bifurcation-like diagram by plotting the post-transient oscillation amplitude of the viral load V against the intracellular delay τ, while fixing the immune delay $\tau_p = 5$ days. Figure 2 shows that the amplitude remains near zero for small delays and then increases in a step-like manner as τ grows, with noticeable rises around $\tau \approx 28$–30 days and $\tau \approx 37$–39 days under the baseline parameter set (Table 1). However, these amplitudes are extremely small in magnitude and should be interpreted as a coarse numerical screening rather than direct evidence of sustained oscillations or true delay-driven regime transitions. In particular, because the sweep is coarse (2-day increments) and the explicit Euler discretization provides limited resolution, the apparent step-like features may reflect discretization or sampling effects and sensitivity near the numerical noise floor. Accordingly, we treat Figure 2 as an exploratory scan that identifies delay ranges warranting higher-resolution verification.

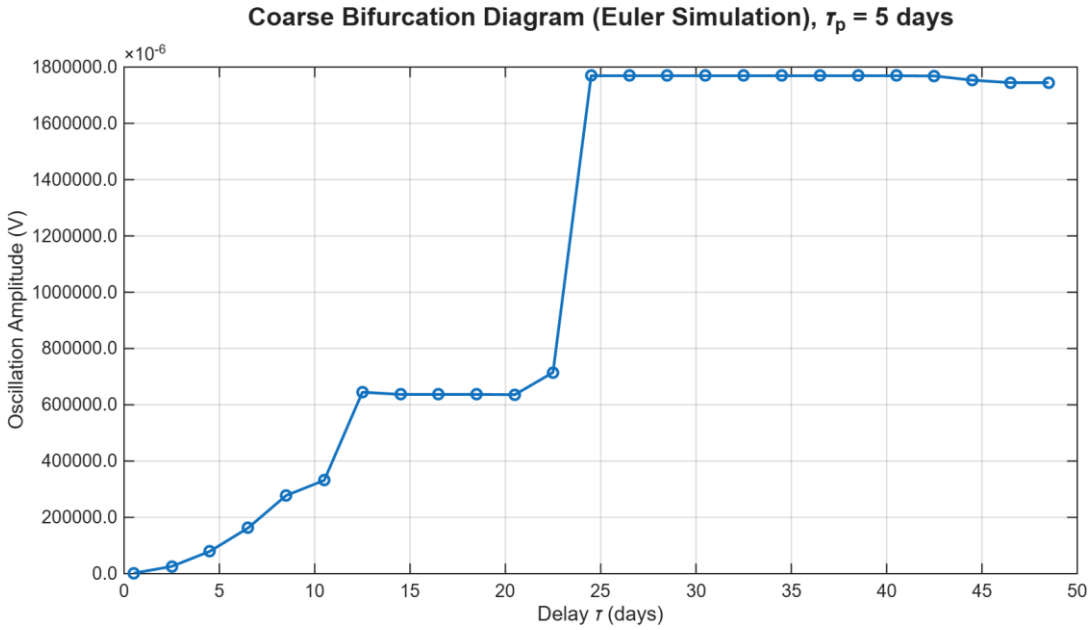

Figure 2. Coarse bifurcation-like diagram showing the post-transient oscillation amplitude of the viral load V versus the intracellular delay τ for a fixed immune delay $\tau_p = 5$ days, used as a low-resolution numerical screening prior to the high-resolution dde23 sweep in Section 5.3.

From a dynamical perspective, the increase of oscillation amplitude with respect to the intracellular delay suggests that larger delays tend to weaken the stabilizing feedback of the immune response and viral clearance mechanisms. As the delay grows, the system may approach a critical threshold where the endemic equilibrium loses stability and oscillatory behavior can emerge. Although the coarse resolution does not allow us to precisely determine the bifurcation point, the observed amplitude growth indicates delay regions where such transitions are more likely to occur. Therefore, this coarse diagram provides a preliminary numerical indication that intracellular delays may influence the stability structure of the HIV-CTL system and potentially contribute to oscillatory viral dynamics. These delay intervals are subsequently examined using a higher-resolution delay sweep based on MATLAB's dde23 solver in Section 5.3 to confirm whether persistent post-transient oscillations occur beyond the numerical detection level.

A fixed-step Euler scheme was used with step size $h = 0.5$ day and total simulation time $T = 50$ days, and the oscillation amplitude was computed as the max-min of V over the post-transient window after discarding the initial transient portion of each simulation. The delay τ was swept from 0.5 to 50 days in 2-day increments. This coarse scan is interpreted as an exploratory numerical screening, and its qualitative features were found to be consistent with finer Euler discretization.

5.3. High-resolution delay sweep (dde23)

To examine whether the step-like increases observed in the coarse Euler screening (Section 5.2) indicate any detectable delay-driven oscillations, we performed a refined, high-resolution delay sweep using MATLAB's built-in dde23 solver. In accordance with the transition bands suggested by Figure 2, the intracellular delay τ was scanned on two focused intervals: [27,31] days and [31,41] days, with

increment $\Delta\tau = 0.5$ days. The immune-activation delay was fixed at its baseline value $\tau_p = 5$ days (Table 1). For each τ, systems (1.1)–(1.5) was integrated over $t \in [0, T]$ with $T = 1000$ days using representative solver settings (absolute tolerance 10^{-6}, relative tolerance 10^{-4}, and maximum step size of 1 day). The history functions on $[-\max(\tau, \tau_p), 0]$ were taken at the infection-free equilibrium $(S_0, I_0, V_0, P_0, A_0)$. To quantify post-transient oscillatory behavior of the viral load, we evaluated the oscillation amplitude over the stabilized window $[T_0, T]$ with $T_0 = 500$ days as

$$A_{osc}(\tau) = \max_{t\in[T_0,T]} V(t) - \min_{t\in[T_0,T]} V(t). \tag{5.3}$$

Because very small nonzero amplitudes may arise from numerical noise, we introduced a practical detection threshold $\varepsilon = 10^{-8}$ and interpret oscillations as numerically detectable only when $A_{\mathrm{osc}}(\tau) > \varepsilon$. As shown in Figure 3 (logarithmic vertical axis), $A_{\mathrm{osc}}(\tau)$ remains at the numerical noise floor across both refined intervals and stays well below ε. Therefore, the step-like changes suggested by the coarse Euler screening in Section 5.2 are not confirmed as sustained, detectable oscillations under the baseline parameter set; within these physiologically relevant ranges, any delay-induced oscillatory component—if present—is extremely small and indistinguishable from numerical noise at the tested resolution. High-resolution delay sweep of the post-transient oscillation amplitude $A_{\mathrm{osc}}(\tau)$ of the free-virus load $V(t)$ versus the intracellular delay τ, computed using MATLAB's dde23 with $\tau_p = 5$ days and evaluated on the post-transient window $[T_0, T] = [500,1000]$.

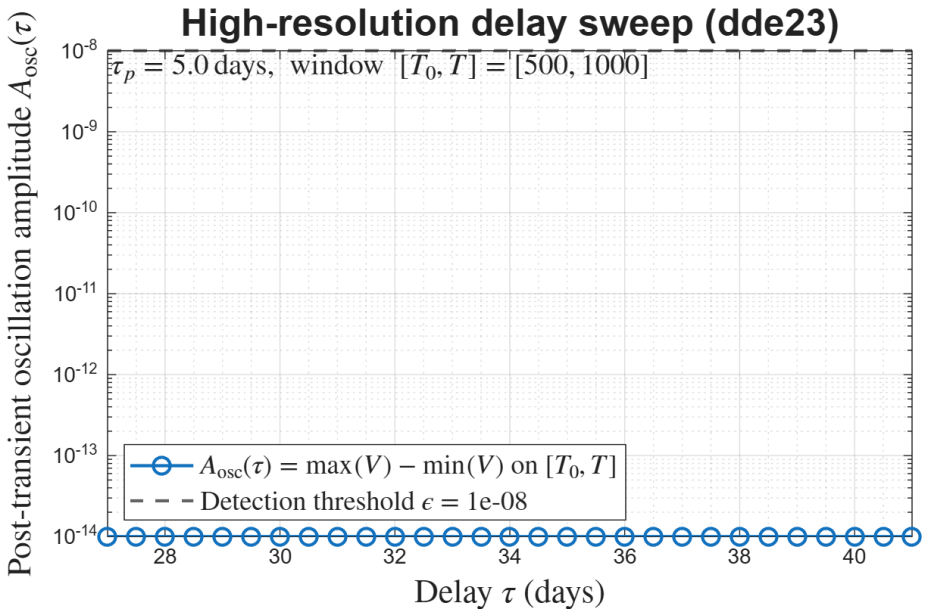

Figure 3. High-resolution delay sweep (dde23): post-transient oscillation amplitude $A_{\mathrm{osc}}(\tau)$ of the viral load $V(t)$ versus the intracellular delay τ for $\tau_p = 5$ days.

The dashed line denotes the detection threshold $\varepsilon = 10^{-8}$. For all scanned τ, $A_{\mathrm{osc}}(\tau)$ remains at the numerical noise floor (or below) and well below ε, indicating no detectable sustained delay-driven oscillations; hence the step-like changes suggested by the coarse Euler screening (Section 5.2) are not confirmed under the baseline parameter set.

5.4. Two-parameter stability analysis in the (τ, τ_p) plane

To extend the one-dimensional delay sweeps in Sections 5.2 and 5.3, we constructed a two-parameter stability map by simultaneously varying the intracellular infection delay τ and the immune activation delay τ_p. For each parameter pair (τ, τ_p), the delay system was simulated over a fixed time horizon $[0, T]$. To exclude transient effects, we discarded the initial portion of the trajectory and quantified oscillatory behavior only on the post-transient window $[T_0, T]$, consistent with the amplitude definition used in Sections 5.2–5.3. We define the post-transient oscillation amplitude of the free-virus load $V(t)$ as

$$A_{osc}(\tau, \tau_p) = \max_{t\in[T_0,T]} V(t) - \min_{t\in[T_0,T]} V(t), \tag{5.4}$$

and assemble $A_{\mathrm{osc}}(\tau, \tau_p)$ over the (τ, τ_p) grid to form the two-dimensional stability map shown in Figure 4, displayed on a logarithmic color scale for visibility of very small amplitudes.

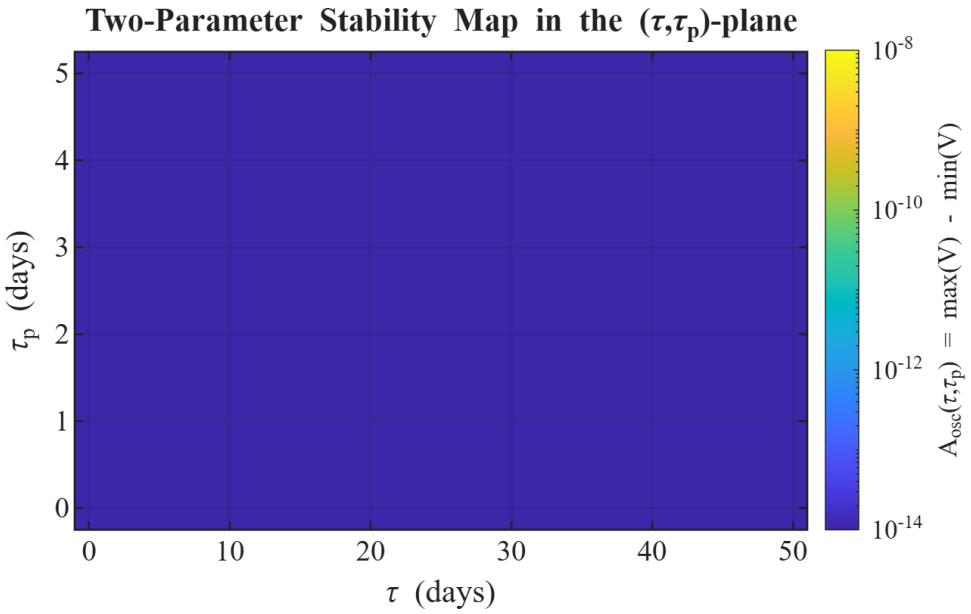

Figure 4. Two-parameter stability map of the post-transient oscillation amplitude of the free-virus load $V(t)$ in the (τ, τ_p) plane.

5.4.1. Results of the two-parameter analysis

Figure 4 shows the resulting amplitude map in the (τ, τ_p) plane. Across the explored domain, the computed post-transient amplitudes remain extremely small and stay at (or below) the numerical detection level used in the one-parameter sweeps. No region of appreciable oscillation growth is observed, and no qualitative transition from steady-state convergence to sustained periodic behavior emerges as τ and τ_p vary simultaneously. These findings indicate that, under the baseline parameter set in Table 1, the endemic equilibrium is numerically robust with respect to coupled variations in both delays within the investigated physiological ranges.

5.4.2. Interpretation

Biologically, this robustness suggests that plausible variations in the intracellular production delay and CTL activation delay do not meaningfully destabilize the long-term viral–immune dynamics under baseline conditions. While delays can modulate transient trajectories, the combined immune-mediated clearance and viral removal mechanisms remain sufficiently strong to drive the system toward a stable chronic-state equilibrium. Mathematically, these results support the conclusion that the stability landscape in the considered domain is dominated by the non-delayed feedback structure and does not exhibit a detectable delay-induced Hopf-type transition within the scanned (τ, τ_p) region. This numerical observation is consistent with the high-resolution one-parameter sweep in Section 5.3, where post-transient oscillation amplitudes remained below the prescribed detection threshold.

For each pair (τ, τ_p), the oscillation amplitude was computed as

$$A_{\mathrm{osc}}(\tau, \tau_p) = \max_{t\in[T_0,T]} V(t) - \min_{t\in[T_0,T]} V(t)$$

on the post-transient window $[T_0, T]$. The amplitudes are visualized on a logarithmic color scale to resolve very small values. Across the explored domain, no region of sustained oscillations is detected, indicating numerically robust convergence to a non-oscillatory steady state under simultaneous variations of both delays.

5.5. Sensitivity analysis

To assess which model parameters most strongly influence the long-term viral burden, we performed a global sensitivity screening focusing on four key kinetic parameters: the infection rate β, the activated-CTL death rate κ, the CTL activation rate σ, and the viral clearance rate c. We generated $N = 100$ parameter sets using Latin hypercube sampling (LHS) within the biologically plausible bounds listed in Table 1. For each sampled parameter set, the systems (1.1)–(1.5) was integrated over $t \in [0,50]$ days using a fixed-step Euler scheme with step size $h = 0.5$ day. To reduce the influence of transient dynamics, the first 25 days were treated as burn-in and excluded from the summary statistics. For each simulation, the mean viral load was computed over the post-transient window as

$$\overline{V} = \frac{1}{T-t_b}\int_{t_b}^{T} V(t)\ dt,\ t_b = 25,\ T = 50 \tag{5.5}$$

implemented numerically by averaging the discrete solution values of $V(t)$ on [25,50]. To quantify the relative influence of each parameter on $\bar{V}$, we computed the squared Pearson correlation coefficient,

$$R_j^2 = \left(\mathrm{corr}\left(\theta_j, \bar{V}\right)\right)^2, \tag{5.6}$$

where $\mathrm{corr}(\cdot,\cdot)$ denotes the Pearson correlation coefficient between the sampled parameter $\theta_j \in \{\beta, \kappa, \sigma, c\}$ and the corresponding mean viral load $\bar{V}$ across the LHS samples. These R^2 values provide an approximate first-order screening index and are used here primarily to rank parameters by their marginal association with mean viral load. The results (Table 2) indicate that the infection rate β

and the CTL activation rate σ exhibit the strongest influence on the mean viral load, with the highest R^2 values. In contrast, the activated-CTL death rate κ and the viral clearance rate c show weaker associations within the explored ranges. Overall, this screening suggests that infection efficiency (β) and CTL activation dynamics (σ) are the dominant drivers of viral persistence under the baseline regime, and therefore represent key targets for parameter refinement and future model-based investigations.

Table 2. Approximate first-order sensitivity indices (R^2) for four key parameters obtained from Latin hypercube sampling and Euler-based simulations of the mean viral load.

Parameter	R^2
β (infection rate)	0.82
κ (activated-CTL death rate)	0.27
σ (CTL activation rate)	0.75
c (viral clearance rate)	0.19

5.6. Robustness analysis

To assess the numerical robustness of the conclusions drawn from the bifurcation and stability-map investigations in Sections 5.2–5.4, we carried out consistency checks focusing on solver tolerances and time discretization. Across these tests, the qualitative stability patterns were preserved and the computed oscillation amplitudes remained numerically near zero within the displayed scales. First, the refined delay sweeps in Section 5.3 were repeated using tighter dde23 tolerance settings. The post-transient oscillation amplitudes remained at the numerical noise floor (approximately 10^{-14}) and well below the practical detection threshold $\varepsilon = 10^{-8}$ throughout the scanned delay intervals. No detectable sustained oscillations emerged under the tighter tolerance settings, indicating that the refined numerical conclusions are insensitive to reasonable tolerance refinement. Second, the coarse Euler-based scans were recomputed using multiple step sizes, including $h = 1.0,\ 0.5,\ 0.25,$ and 0.1 days. The results for the finer step sizes $h = 0.5,\ 0.25,$ and 0.1 showed qualitatively similar step-like amplitude patterns, whereas the coarsest discretization $h = 1.0$ produced markedly distorted amplitudes, indicating that this step size is too coarse for reliable screening. Accordingly, the coarse bifurcation-like diagram is interpreted using the finer Euler discretizations, which provide more stable qualitative behavior while remaining computationally inexpensive. Overall, these checks support the conclusion that the numerical results reported in Sections 5.2–5.4 are robust with respect to the main solver and discretization settings considered here, and that the reported near-zero oscillation amplitudes are not artifacts of a particular numerical configuration.

6. Discussion

This work integrates analytical stability theory with refined delay-differential simulations to clarify how the intracellular infection delay and the CTL-activation delay influence within-host HIV-CTL dynamics. The analysis establishes positivity and boundedness of solutions, characterizes the

infection-free equilibrium E_0 and the endemic equilibrium E^*, and derives delay-dependent stability conditions together with a Hopf-type transition criterion for the endemic state. Numerical investigations complement these results by quantifying the delay response of long-term viral behavior using the post-transient oscillation amplitude of the viral load as the main numerical output. Across the physiologically relevant ranges explored under the baseline parameter set, solutions converge to a non-oscillatory chronic state and the computed oscillation amplitudes remain numerically near zero, indicating no detectable sustained oscillations in the scanned regions. From a dynamical perspective, the coarse Euler scans suggest that increasing the intracellular delay may move the system closer to potential stability boundaries. However, the refined dde23 computations show that, for the baseline parameter regime considered here, these apparent transitions are not confirmed as detectable sustained oscillations and remain at the numerical noise floor. Likewise, the two-parameter stability map in the (τ, τ_p)-plane indicates numerically robust convergence across the investigated delay domain. Thus, the analytical framework identifies mechanisms through which delay-induced instability may in principle occur, whereas the numerical results show that such transitions are not realized within the tested baseline parameter set and physiological delay ranges. Sensitivity screening further identifies the infection rate β and the CTL activation rate σ as the dominant drivers of long-term viral burden, whereas the viral clearance rate c and the activated-CTL death rate κ exhibit weaker marginal associations within the explored ranges. These findings highlight that infection efficiency and immune activation dynamics are key determinants of long-term viral persistence in the present model. In addition, the main qualitative conclusions are preserved under refinement of the dde23 solver tolerances and under finer Euler step sizes in the coarse delay scan, supporting the numerical robustness of the reported non-oscillatory baseline behavior. Unlike earlier HIV-CTL delay models that often include only a single discrete delay or rely on more aggregated delay effects, the present framework incorporates two biologically interpretable delays and provides a transparent structure for analyzing their combined influence. In particular, the model separates the role of the intracellular infection delay from that of the immune-activation delay, allowing analytical identification of delay-dependent stability conditions while also showing numerically that, under the chosen baseline conditions, the long-term dynamics remain close to a stable endemic regime.

6.1. Biological and clinical implications

The results suggest that intracellular timing can act as a mechanistic modulator of viral persistence, even when overt sustained oscillations are not numerically detected under baseline conditions. Delays associated with intracellular eclipse or replication processes may bring the system closer to stability boundaries, thereby altering the transient viral response and potentially increasing susceptibility to oscillatory behavior under perturbed parameter regimes. In parallel, effective CTL activation remains central to controlling long-term viral burden, as reflected by the strong sensitivity of the model to the activation parameter σ. More broadly, the analysis indicates that therapeutic strategies targeting both viral replication kinetics and immune response efficiency may help maintain stable long-term suppression of infection.

6.2. Limitations and future directions

This study adopts fixed discrete delays and assumes spatially homogeneous mixing between virus and immune populations, which simplifies within-host heterogeneity. Extensions to distributed or state-dependent delays could provide a closer representation of variability in intracellular processing and immune activation, while spatially structured formulations may capture localized viral–immune interactions that are not represented in a well-mixed setting. In addition, the present numerical bifurcation results are tied to the chosen baseline parameter set and scanned physiological ranges; although the analytical theory allows delay-induced instability in principle, broader parameter exploration may be needed to identify regimes in which numerically detectable sustained oscillations occur. From a translational perspective, coupling the current framework with PK-PD components could provide a more direct link between dosing schedules, drug exposure profiles, and delay-mediated viral dynamics. Patient-informed parameter inference and individualized simulations may further support subject-specific treatment design and improve timing strategies for durable viral suppression.

7. Conclusions

We presented a dual-delay HIV-CTL framework that combines analytical stability theory with numerical delay sweeps, bifurcation-like screening, sensitivity analysis, and targeted robustness checks. The results show that the intracellular infection delay and the CTL-activation delay provide a meaningful mathematical structure for studying long-term viral-immune interactions, while the baseline parameter regime considered here remains numerically stable and non-oscillatory across the investigated delay ranges. The analytical results indicate that delay-induced instability and Hopf-type transitions may arise under appropriate parameter conditions, but the refined numerical evidence shows that such transitions are not detected within the baseline setting examined in this work. These findings provide a structured foundation for future studies involving richer delay formulations, broader parameter exploration, alternative immune-efficacy mechanisms, and patient-informed calibration aimed at improving strategies for long-term viral suppression.

Author contributions

S. Suksai conceived the study, formulated the model, performed the theoretical analysis, developed the computational code, conducted numerical simulations, interpreted the results, and drafted and revised the manuscript. S. Suantai contributed to the study design, supervised the research, secured funding (with S. Suksai), and critically revised the manuscript. A. Tamsat supported the computational experiments. C. Salikupata contributed to the sensitivity analysis and robustness checks. All authors reviewed and approved the final manuscript.

Funding

This research was supported by the Science, Research, and Innovation Promotion Fund (SRF) under the Fundamental Fund for Fiscal Year 2025 through Srinakharinwirot University (Contract No. 040/2568). The second author (Suthep Suantai) was also supported by Chiang Mai University.

Data accessibility statement

All data and simulation code supporting this study are provided in this article and its electronic supplementary material. The MATLAB scripts used for the numerical simulations and bifurcation analyses are included as supplementary files. Additional details are available from the corresponding author upon reasonable request (sayaphat@g.swu.ac.th).

Ethical statement

This study is based solely on mathematical and computational modeling and does not involve human participants, human biological specimens, or individual-level human data. The Human Research Ethics Committee of Srinakharinwirot University granted an exemption (Protocol: SWUEC-671111; approval date: 16 December 2024; expiry date: 15 December 2027).

Human data statement

No prospective recruitment was undertaken and no retrospective use of medical records, archived samples, or human survey datasets was performed for this research.

Use of Generative-AI tools declaration

The authors used artificial intelligence tools for language editing and proofreading only. The scientific content and conclusions were developed entirely by the authors.

Conflict of interest

All authors declare no conflicts of interest in this paper.

References

1. A. S. Perelson, R. M. Ribeiro, Modeling the within-host dynamics of HIV infection, *BMC Biol.*, **11** (2013), 96. https://doi.org/10.1186/1741-7007-11-96
2. M. A. Nowak, C. R. M. Bangham, Population dynamics of immune responses to persistent viruses, *Science*, **272** (1996), 74–79. https://doi.org/10.1126/science.272.5258.74
3. S. Bonhoeffer, R. M. May, G. M. Shaw, M. A. Nowak, Virus dynamics and drug therapy, *Proc. Natl. Acad. Sci. USA*, **94** (1997), 6971–6976. https://doi.org/10.1073/pnas.94.13.6971
4. X. Wei, S. K. Ghosh, M. E. Taylor, V. A. Johnson, E. A. Emini, P. Deutsch, et al., Viral dynamics in human immunodeficiency virus type 1 infection, *Nature*, **373** (1995), 117–122. https://doi.org/10.1038/373117a0
5. S. J. Little, A. R. McLean, C. A. Spina, D. D. Richman, D. V. Havlir, Viral dynamics of acute HIV-1 infection, *J. Exp. Med.*, **190** (1999), 841–850. https://doi.org/10.1084/jem.190.6.841
6. C. L. Althaus, R. J. de Boer, Dynamics of immune escape during HIV/SIV infection, *PLoS Comput. Biol.*, **4** (2008), e1000103. https://doi.org/10.1371/journal.pcbi.1000103

7. C. L. Althaus, S. Bonhoeffer, Stochastic interplay between mutation and recombination during the acquisition of drug resistance mutations in human immunodeficiency virus type 1, *J. Virol.*, **79** (2005), 13572–13578. https://doi.org/10.1128/JVI.79.21.13572-13578.2005
8. S. Sukegawa, H. Takeuchi, Toward the unveiling of HIV-1 dynamics: involvement of monocytes/macrophages in HIV-1 infection, *Front. Virol.*, **2** (2022), 934892. https://doi.org/10.3389/fviro.2022.934892
9. D. Wodarz, D. N. Levy, Human immunodeficiency virus evolution towards reduced replicative fitness in vivo and the development of AIDS, *Proc. Biol. Sci.*, **274** (2007), 2481–2490. https://doi.org/10.1098/rspb.2007.0413
10. S. J. Krebs, J. Ananworanich, Immune activation during acute HIV infection and the impact of early antiretroviral therapy, *Curr. Opin. HIV AIDS*, **11** (2016), 163–172. https://doi.org/10.1097/COH.0000000000000228
11. B. A. Larder, The influence of combination therapy on HIV-1 viral load and drug resistance, *AIDS*, **8** (1994), 1559–1563. https://doi.org/10.1097/00002030-199411004-00013
12. D. V. Havlir, D. D. Richman, The role of viral dynamics in the pathogenesis of HIV disease and implications for antiviral therapy, *Springer Semin. Immun.*, **18** (1997), 267–283. https://doi.org/10.1007/BF00813498
13. G. A. Bocharov, A. A. Romanyukha, Mathematical model of antiviral immune response. III. Influenza A virus infection, *J. Theor. Biol.*, **167** (1994), 323–360. https://doi.org/10.1006/jtbi.1994.1074
14. D. Kirschner, G. F. Webb, A model for treatment strategy in the chemotherapy of AIDS, *Bull. Math. Biol.*, **58** (1996), 367–390. https://doi.org/10.1007/BF02458312
15. P. W. Nelson, J. D. Murray, A. S. Perelson, A model of HIV-1 pathogenesis that includes an intracellular delay, *Math. Biosci.*, **163** (2000), 201–215. https://doi.org/10.1016/S0025-5564(99)00055-3
16. J. E. Mittler, R. Sulzer, A. U. Neumann, A. S. Perelson, Influence of delayed viral production on viral dynamics in HIV-1 infected patients, *Math. Biosci.*, **152** (1998), 143–163. https://doi.org/10.1016/S0025-5564(98)10027-5
17. D. Kirschner, M. R. Mehr, A. S. Perelson, Role of the thymus in pediatric HIV-1 infection, *J. Acq. Imm. Def.*, **18** (1998), 95–109. https://doi.org/10.1097/00042560-199806010-00001
18. P. W. Nelson, G. Gilchrist, D. Coombs, J. M. Hyman, A. S. Perelson, An age-structured model of HIV infection that allows for variations in the production rate of viral particles and the death rate of productively infected cells, *Math. Biosci. Eng.*, **1** (2004), 267–288. https://doi.org/10.3934/mbe.2004.1.267
19. S. M. Messinger, A. Ostling, The consequences of spatial structure for the evolution of pathogen transmission rate and virulence, *Am. Nat.*, **174** (2009), E128–E141. https://doi.org/10.1086/605375
20. P. van den Driessche, J. Watmough, Reproduction numbers and sub-threshold endemic equilibria for compartmental models of disease transmission, *Math. Biosci.*, **180** (2002), 29–48. https://doi.org/10.1016/S0025-5564(02)00108-6
21. R. M. Ribeiro, L. Qin, L. L. Chavez, D. Li, S. G. Self, A. S. Perelson, Estimation of the initial viral growth rate and basic reproduction number during acute HIV-1 infection, *J. Virol.*, **84** (2010), 6096–6102. https://doi.org/10.1128/JVI.00127-10

22. S. Alizon, C. Fraser, Within-host and between-host evolutionary rates across the HIV-1 genome, *Retrovirology*, **10** (2013), 49. https://doi.org/10.1186/1742-4690-10-49
23. A. N. Phillips, HIV viral load response to antiretroviral therapy according to baseline CD4 cell count and viral load, *JAMA*, **286** (2001), 2560–2567. https://doi.org/10.1001/jama.286.20.2560
24. M. A. Stafford, L. Corey, J. Cao, Z. S. Daar, H. D. Ho, A. S. Perelson, Modeling plasma virus concentration during primary HIV infection, *J. Theor. Biol.*, **203** (2000), 285–301. https://doi.org/10.1006/jtbi.2000.1076
25. L. Rong, A. S. Perelson, Modeling latently infected cell activation: viral and latent reservoir persistence, and viral blips in HIV-infected patients on potent therapy, *PLoS Comput. Biol.*, **5** (2009), e1000533. https://doi.org/10.1371/journal.pcbi.1000533
26. J. M. Conway, D. Coombs, A stochastic model of latently infected cell reactivation and viral blip generation in treated HIV patients, *PLoS Comput. Biol.*, **7** (2011), e1002033. https://doi.org/10.1371/journal.pcbi.1002033
27. J. M. Conway, A. S. Perelson, Post-treatment control of HIV infection, *Proc. Natl. Acad. Sci. USA*, **112** (2015), 5467–5472. https://doi.org/10.1073/pnas.1419162112
28. R. J. de Boer, A. S. Perelson, Quantifying T lymphocyte turnover, *J. Theor. Biol.*, **327** (2013), 45–87. https://doi.org/10.1016/j.jtbi.2012.12.025
29. A. Korobeinikov, Global properties of infectious disease models with nonlinear incidence, *Bull. Math. Biol.*, **69** (2007), 1871–1886. https://doi.org/10.1007/s11538-007-9196-y
30. S. Beretka, G. Vas, Saddle-node bifurcation of periodic orbits for a delay differential equation, *J. Differ. Equ.*, **269** (2020), 4215–4252. https://doi.org/10.1016/j.jde.2020.03.039
31. S. Han, C. Lei, Global stability of equilibria of a diffusive SEIR epidemic model with nonlinear incidence, *Appl. Math. Lett.*, **98** (2019), 114–120. https://doi.org/10.1016/j.aml.2019.05.045
32. K. Gopalsamy, *Stability and oscillations in delay-differential equations of population dynamics*, New York: Springer-Verlag, 1992. https://doi.org/10.1007/978-94-015-7920-9
33. S. Ruan, Delay-differential equations in single species dynamics, In: *Delay-differential equations and Applications*, Dordrecht: Springer, 2006. https://doi.org/10.1007/1-4020-3647-7_11
34. Z. Hu, J. Yang, L. Lv, Q. Li, D. Fan, Dynamics analysis of a delayed HIV-1 model with general incidence rate and immune impairment, *Math. Comput. Simul.*, **241** (2026), 137–164. https://doi.org/10.1016/j.matcom.2025.09.021
35. D. Hu, Y. Yuan, Threshold dynamics of an age-structured HIV model with virus-to-cell, cell-to-cell transmissions, and CTL immune response, *J. Math. Biol.*, **92** (2026), 13. https://doi.org/10.1007/s00285-025-02328-4
36. J. K. Hale, S. M. Verduyn Lunel, *Introduction to functional differential equations*, New York: Springer, 1993. https://doi.org/10.1007/978-1-4612-4342-7

AIMS Press